ACS APPLIED MATERIALS & INTERFACES

www.acsami.org Research Article

Three-Dimensional Graphene Sheet-Carbon Veil Thermoelectric Composite with Microinterfaces for Energy Applications

Vamsi Krishna Reddy Kondapalli, Oluwasegun Isaac Akinboye, Yu Zhang, Guillaume Donadey, Justin Morrow, Kyle Brittingham, Ayush Arun Raut, Mahnoosh Khosravifar, Bashar Al-Riyami, Je-Hyeong Bahk, and Vesselin Shanov*

Cite This: *ACS Appl. Mater. Interfaces* 2024, 16, 13150−13160 Read Online

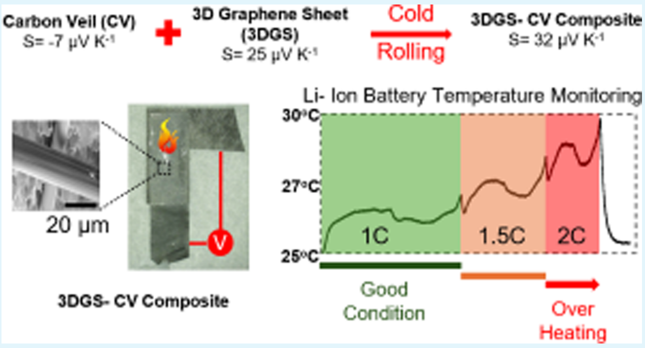

ABSTRACT: Over the years, various processing techniques have been explored to synthesize three-dimensional graphene (3DG) composites with tunable properties for advanced applications. In this work, we have demonstrated a new procedure to join a 3D graphene sheet (3DGS) synthesized by chemical vapor deposition (CVD) with a commercially available carbon veil (CV) via cold rolling to create 3DGS-CV composites. Characterization techniques such as scanning electron microscopy (SEM), Raman mapping, X-ray diffraction (XRD), electrical resistance, tensile strength, and Seebeck coefficient measurements were performed to understand various properties of the 3DGS-CV composite. Extrusion of 3DGS into the pores of CV with multiple microinterfaces between 3DGS and the graphitic fibers of CV was observed, which was facilitated by cold rolling. The extruded 3D graphene revealed pristine-like behavior with no change in the shape of the Raman 2D peak and Seebeck coefficient. Thermoelectric (TE) power generation and photothermoelectric responses have been demonstrated with in-plane TE devices of various designs made of p-type 3DGS and n-type CV couples yielding a Seebeck coefficient of 32.5 $\mu V\ K^{-1}$. Unlike various TE materials, 3DGS, CV, and the 3DGS-CV composite were very stable at high relative humidity. The 3DGS-CV composite revealed a thin, flexible profile, good moisture and thermal stability, and scalability for fabrication. These qualities allowed it to be successfully tested for temperature monitoring of a Li-ion battery during charging cycles and for large-area temperature mapping.

KEYWORDS: *3D graphene sheet, carbon veil, cold rolling, flexible thermoelectric, photothermoelectric, thermocouples*

1. INTRODUCTION

Since its discovery in 2004, graphene has been a highly studied nanomaterial due to its exceptional properties. Various synthesis techniques were explored to enhance the quality and quantity of graphene.[1,2] Two-dimensional (2D) graphene materials like graphene, graphene oxide (GO), and reduced graphene oxide (rGO) have been used as reinforcing agents in metals, polymers, ceramics, or a mixture of materials.[3,4] Alternatively, graphene-coated composites have been synthesized by depositing graphene directly on three-dimensional (3D) metal alloy catalysts and ceramic substrates.[5−7] These composites demonstrated enhanced electrical, mechanical, electrochemical, and thermal properties when compared to the base materials but suffer from the requirement for larger chemical vapor deposition (CVD) systems. The bonding between graphene materials and the matrix phase plays a crucial role in the properties of the above-mentioned composites. Interfacial bonding including $\pi-\pi$ and electrostatic interactions, hydrogen bonding, and mechanical keying/interlocking is the most common means of bonding between graphene materials and the matrix phase where covalent bonding was also found in a small number of polymer-graphene composites.[3,8,9]

Due to the 2D nature of graphene, agglomeration, stacking, and nonuniform distribution were observed, thus decreasing the effectiveness of graphene in these composites. Large variations in the properties across the dimensions of the composites and between composites from the same batch were observed.[3,10] Alternatively, graphene-laminated composites were developed by transferring large-area CVD synthesized graphene or laser-induced graphene onto polymers or metals via a simple lamination process involving folding or

Received: January 2, 2024
Revised: February 20, 2024
Accepted: February 21, 2024
Published: March 4, 2024

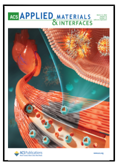

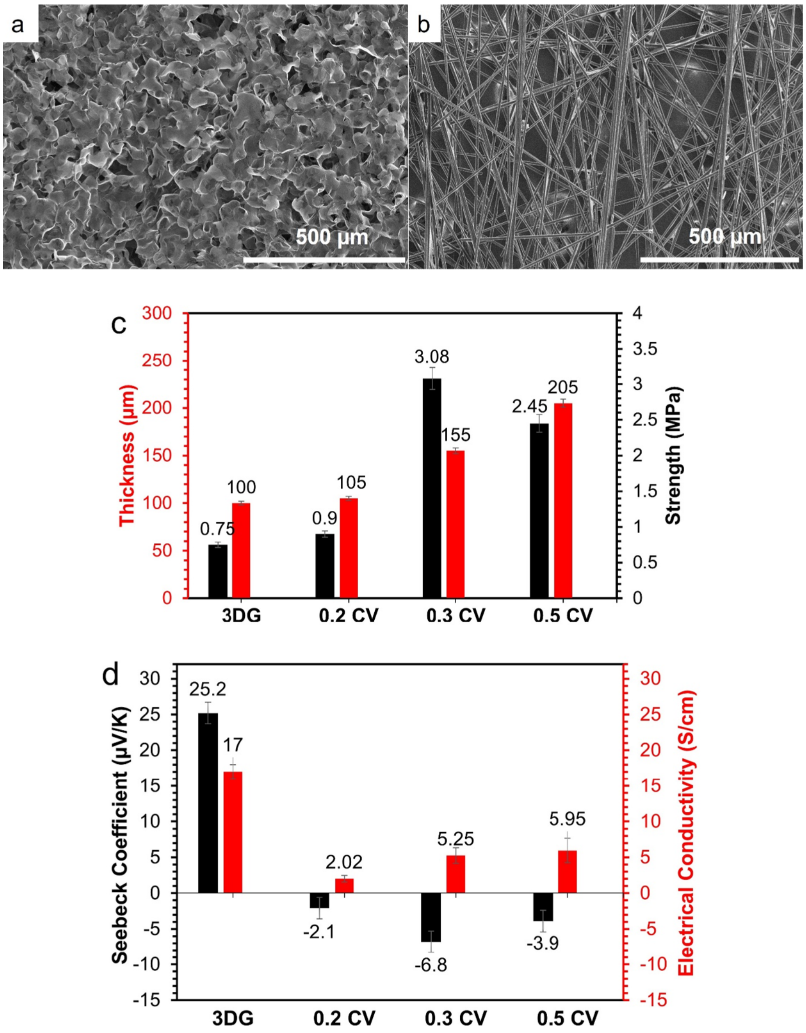

Figure 1. SEM image of (a) 3DGS; (b) 0.3 g/cm^3 carbon veil. Plots comparing (c) thickness and strength and (d) electrical conductivity and Seebeck coefficient of 3DGS and CVs of various densities 0.2 g/cm^3 (0.2 CV), 0.3 g/cm^3 (0.3 CV), and 0.5 g/cm^3 (0.5 CV).

compression with heat. The layer structure can be repeated according to the requirement, thus altering the properties. The laminated composites demonstrated superior tensile strength and electrical conductivity.[11−13]

Highly porous and lightweight 3D graphene monoliths like foams, aerogels, and hydrogels with graphene flakes held together via covalent linkages or hydrogen bonding can overcome all the issues faced by 2D graphene.[14−16] Graphene foam possesses superior electrical and thermal properties than its graphene 3D counterparts but it is mechanically weak.[17] Techniques like dip coating/casting, electro- and electroless deposition, electrostatic spray deposition, vacuum infiltration, etc. were used to incorporate polymers in 3D graphene.[8] Metals and ceramics were deposited on 3D graphene materials via electro- and electroless deposition, hydrothermal, and solvothermal techniques.[3,9] Various 3D graphene composites were synthesized via freeze-drying or 3D printing of graphene-based solutions stabilized by polymers.[8]

In our recent work, we demonstrated the ability of our CVD-synthesized 3D graphene to accommodate stress via extrusion. 3D graphene behaved like a bulk material and demonstrated no cracks or failure under compressive stress.[18] Based on the found extrusion property theoretically, 3D graphene can be joined with any porous material by cold rolling together without the requirement for a high temperature or chemical processing. In this work, we test this hypothesis by joining a CVD-synthesized 3D graphene sheet (3DGS) with a highly porous commercial carbon veil (CV) via simple cold rolling. The expectation is that 3DGS extruded into the pores of CV will create good interfacial bonding, thus resulting in a new material called 3DGS-CV composites. For exploring potential advanced applications of this material, a wide variety of characterization techniques were employed, which were expected to help us understand the ultimate properties of these composites. Testing the effect of various structural aspects on the photothermal, thermoelectric, and photothermoelectric behavior of 3DGS-CV composites with potential applications in temperature sensing and mapping is an additional objective of this work.

2. EXPERIMENTAL SECTION

2.1. Material Characterization. Scanning electron microscopy (SEM) images of composites were acquired using an FEI Apreo microscope. The sample cross-sectioning was achieved by a focused ion beam (FIB) using a Ga liquid metal ion source (LMIS), and the respective imaging was acquired by a SCIOS dual beam SEM. A very thin film of platinum was deposited as a mask to secure the cutting of the sample by the FIB within the desired areas. A nanosecond solid-state 532 nm laser milling instrument from Oxford Lasers was used to cut the 3DGS, CV, and composite samples for various characterizations. Rigaku SmartLab XRD system with a Cu Kα radiation source was employed to study the 3DGS and composite samples at room temperature by scanning them within the 2θ range from 10° to 90°. MDI's JADE software was implemented to analyze and identify the peaks in the XRD spectra. The tensile testing of the materials was performed using an Instron 5940 Single Column Frame equipped with a 100 N load cell, where the samples were mounted on a paper frame. Thermogravimetric analysis (TGA) of the samples was conducted using a TA 550 instrument from TA Instruments. Thermal images were captured with an FLIR T640 thermal camera. The sheet resistance was measured using a Delcom 873 Interface Module noncontact instrument. The room temperature in-plane Seebeck coefficient measurements were carried out with a custom-built setup. Detailed step-by-step procedures used to measure the Seebeck coefficient and electrical conductivity are provided in the Supporting Information (SI). The voltage and current measurements and the related data storage were conducted by using Keithley 2450 Source meters.

2.2. Materials and Synthesis of 3DGS. 3DGS was synthesized via a CVD process as described in detail in our previous publication.[16] In brief, a nickel polymer slurry was prepared in two steps. First, 5.5 g of polystyrene (Scientific polymer products *M*w 210,000 GPC) was mixed with 1.6 mL of di(ethylene glycol)dibenzoate (TCI SG 1.18) and 17 mL of toluene (Sigma-Aldrich) in a glass vial followed by heating and continued stirring for 6 h to dissolve the polystyrene and to increase the consistency. About 40 g of nickel powder (3−7 μm from Fisher Scientific) was mixed in parts and hand-stirred to prevent nickel agglomeration and to remove bubbles from the slurry. The slurry was knife-cast on a Teflon block with a cast gap of 1.3 mm. The cast was air-dried for around 8 h and was cut into desired shapes and sizes. The cut nickel−polymer cast was used as catalysts for 3DGS synthesis in an ET 1000 CVD reactor (First Nano). The catalysts were heated from room temperature to 1000 °C at a heating rate of 25 °C/min in an argon (1000 sccm) and hydrogen (325 sccm) gas mixture. After reaching 1000 °C, the reactor was held in the same state for 5 min to stabilize the thermal conditions followed by the introduction of methane (25 sccm) for 10 min. At the end of this step, the samples were cooled to below 100 °C where the obtained nickel−graphene composite was taken out of the reactor followed by etching nickel in a 15 M hydrochloric acid bath. Finally, the sample was rinsed in DI water and ethanol bath followed by drying overnight between Kim wipes thus yielding pristine 3DGS. On the other hand, CV is commercially available with 0.2, 0.3, and 0.5 g/cm^3 densities are purchased from ACP Composites Inc.

3. RESULTS AND DISCUSSION

3.1. Material Characterization of 3DGS-CV Composites.

3DGS is highly porous with graphene flakes arranged in random orientations covalently connected, forming a globular morphology, as shown in the SEM image in Figure 1a. Furthermore, CV is highly porous with graphitic fibers arranged randomly and glued together via a polyester binder. The SEM image of 0.3 g/cm^3 CV is shown in Figure 1b. FTIR spectra of CVs of 0.2, 0.3, and 0.5 g/cm^3 densities are shown in Figure S1 of the SI and compared with carbon paper for reference. Figure S1 confirms the presence of polyester with pronounced signature peaks whose intensities increased with the density of the carbon veil.[19,20]

The structural and transport properties of CV and 3DGS such as thickness, tensile strength, electrical conductivity, and Seebeck coefficient are measured and shown in Figure 1d,c. The stress−strain plot for the 0.3 g/cm^3 CV is shown in Figure S2 of the SI, which highlights two different failure regions. The network of the graphitic fibers starts failing at the end of the proportionality limit, thereby increasing the electrical resistance. The CV was found to elongate further due to the plastic deformation of the polyester binder, followed by complete failure at higher stress. In this work, the graphitic fiber network failure point was considered as the strength of the CV material. CVs of different densities are named 0.2 0.3, and 0.5 CV, where 0.2, 0.3, and 0.5 indicate their densities.

The procedure used to measure the Seebeck coefficient and electrical conductivity is shown in Section S1 (Figures S3 and S4) and Section S2 of the SI. The raw data obtained for the Seebeck measurement of all the materials are displayed in Figure S5 of the SI. As shown in Figure 1d, with an increase in density of CV, electrical conductivity increased while no trend was observed for both tensile strength and Seebeck coefficient. All CVs demonstrated an n-type thermoelectric behavior with a negative Seebeck coefficient. The average Seebeck value of ~(−7) μV/K was obtained for 0.3 CV. Due to the superior properties of 0.3 CV among the CVs; this material was our choice here for the fabrication of 3DGS-CV composites.

A similar rolling compression procedure, as described in our publication was implemented here to create the 3DGS-CV composites.[18] MSK-HRP-01 electric hot rolling press from MTI Corporation was used for rolling compression. 3DGS and CV were arranged in various orientations between two kitchen baking sheets (50 μm thick each) and stainless steel (SS) shims of 50 μm thick each and were cold rolled only once at various rolling gaps. The baking sheets prevented the adhesion of the 3DGS or the composite to the SS shims. Here, the overall thickness of the sandwich (2 SS sheets, 2 baking sheets, 3DGS, and CV) before cold rolling was approximately 450 μm. A schematic illustrating the cold rolling procedure used in this work is shown in Figure 2a. The approach and steps employed for estimating the force during cold rolling compression are shown in Figure S6 and Section S3 of the SI. After cold rolling, the composites were carefully peeled off from the baking sheets.

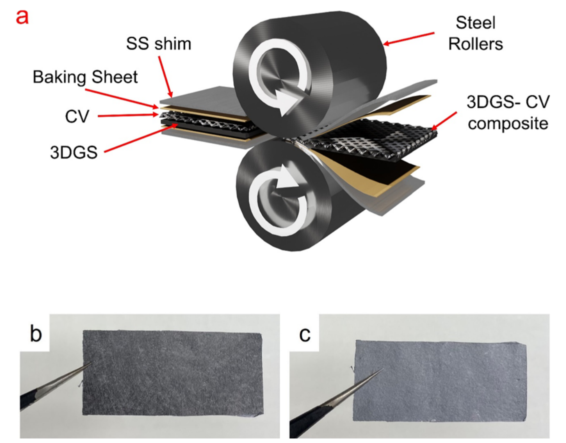

Figure 2. (a) Illustration of the cold rolling process used to create 3DGS-CV composite; (b) CV side of the composite; and (c) 3DGS side of the composite.

A rolling gap lower than 250 μm locally damaged the graphitic fibers in the CV. Furthermore, rolling gaps above 300 μm did not cause extrusion of 3DGS into the pores of CV resulting in a weak bond or no joining between them. As expected, the force experienced by the composite increased with a decrease in the rolling gap. SEM imaging of the composite processed at a 200 μm gap is shown in Figure S7 of the SI revealing multiple failures of the graphitic fibers. Hence, for this study, a rolling gap of 250 μm was chosen to enable the extrusion of 3DGS without damaging the CV. The optical images of the 3DGS-CV composites are shown in Figure 2, where the CV side and the 3DGS side of the composite are displayed in Figure 2b,c, respectively. Both images show a very uniform surface without any damage. The cold rolling parameters used in this study are summarized in Table 1.

Table 1. Parameters Used for Cold Rolling Processing of the 3DGS-CV Composite

parameter	values/details
temperature	room temperature
force	∼12 ± 0.5 N
duration	∼3.3 mm/s
rolling gap	250 ± 10 μm

SEM images on the CV side of the composite at two different magnifications are shown in Figure 3a,b. These images highlight extrusion of 3D graphene into the pores of CV resulting in the formation of interfaces between 3DGS and the graphitic fibers of CV. On the other hand, as shown in the SEM image from the 3DGS side of the composite (Figure 3c), the rough surface morphology of 3DGS displayed in Figure 1a disappeared resulting in a flat surface. The cross-sectional SEM image shown in Figure 3d reveals a graded morphology where more squishing of the pores with high flake alignment can be seen at the bottom. The direction of extrusion is highlighted with a red arrow, where the extruded 3DGS is still porous. This observation suggests that the pores of CV offer stress relief areas for 3DGS thus enabling extrusion. The XRD spectra of the composite shown in Figure S8a support the SEM observations where only 002 and 004 peaks are present due to the domination of graphene flake stacking and alignment. In contrast, randomly oriented graphene flakes are found in 3DGS with multiple XRD peaks in Figure S8b.

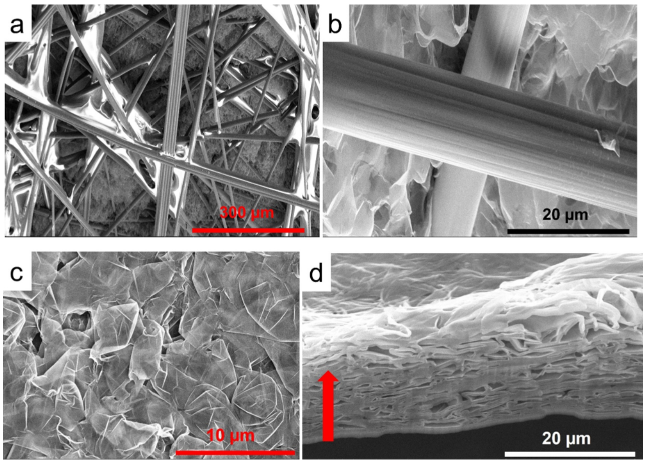

Figure 3. (a) SEM image of the CV side of the 3DGS-CV composite. (b) SEM image of the interface between graphitic fibers and 3DGS. (c) SEM image of the 3DGS side of the composite. (d) FIB-cut cross-section of the 3DGS-CV composite. The red arrow points in the direction of extrusion.

A prototype system from Thermo Fisher Scientific that combines confocal Raman mapping with SEM was used to precisely study the quality of the extruded graphene. A 532 nm laser with a 20× objective and a pixel size of 1 μm^2 was chosen for Raman mapping in a 20 × 20 μm^2 area with 400 spectral points. The SEM image of the mapped area is shown in Figure 3b, where the D/G peak intensity ratio map is shown in Figure 4a. Four different spectra were extracted from different areas of the map and are shown in Figure 4b. Spectra 1 and 4 represent the extruded 3D graphene, and spectra 2 and 3 are from the graphitic fibers. A highly pronounced D peak was observed for the graphitic fibers where, due to the defect-free nature of extruded 3DGS, no D peak or relatively smaller D peak was observed. VOIGT peak fitting of the 2D peak from 1 and 4 spectra was performed and is shown in Figure S9a,b with the related adj. R^2 fit values. The adj. R^2 values of both spectra are greater than 0.98, whereas for compressed graphene, the fit value is less than 0.98, as shown in Figure S9c of the SI. These results corroborated by the SEM observations that the pores in CV acted as stress relief spaces where the extruded graphene preserved its pristine state and did not experience stress accumulation.[15,18,21]

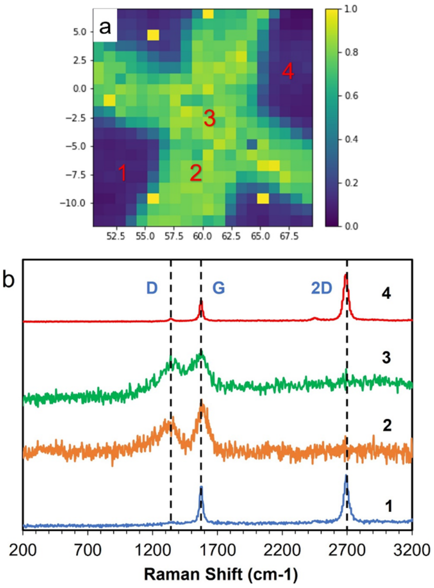

Figure 4. (a) Raman $I(D)/I(G)$ map of the composite. (b) Raman spectra from four different points on the map as pointed out in Figure 4a.

Furthermore, the tensile properties and thermal stability of the 3DGS-CV composite were compared with other materials tested in this work, and the results are shown in Figure 5a and Figure S10 respectively. The tensile strength of 3DGS was lower than that of the other materials due to its high porosity and random alignment of the graphene flakes. 3DGS was compressed between two SS shims at a 100 μm rolling gap followed by dipping in an ethanol bath to separate the compressed 3DGS called here (C3DGS). The latter demonstrated greater tensile strength due to the high alignment of graphene flakes as discussed in detail elsewhere.[18] The blending of 3DGS with CV by cold rolling slightly increased the strength of the resultant material compared with CV alone (from 3.08 to 3.3 MPa). The partial compression and extrusion of 3DGS within the CV lowered the percentage of aligned graphene flakes, thus resulting in a lower strength of 3DGS-CV composite than C3DGS. The TGA data shown in Figure S10 highlights the good thermal stability of 3DGS- CV composite where no weight change was observed till 260°C.

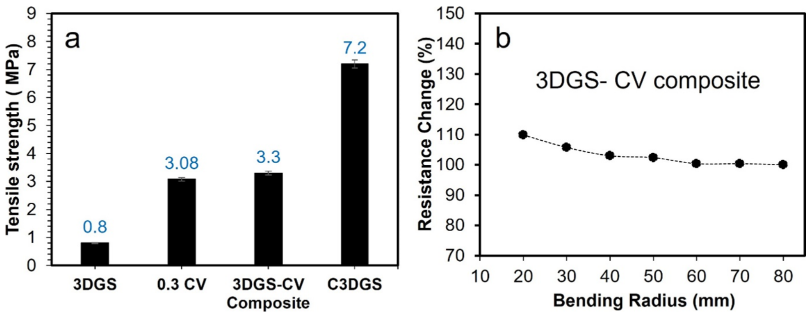

Figure 5. (a) Tensile strength of various materials studied in this work and compared with the 3DGS-CV composite, where C3DGS indicates compressed 3DGS. (b) Effect of bending radius on the electrical resistance of the 3DGS-CV composite.

Both 3DGS and C3DGS are more flexible than CV as the brittle graphitic fibers limit the flexibility of the CV when they bend over a smaller radius of curvatures. As shown in Figure S2 in the SI, the polyester binder kept the CV structure intact after the failure of the graphitic fibers. 3DGS-CV composite of 3 cm × 1 cm in dimensions is bent over a wide range of radiuses and the resistance change is shown in Figure 5b. No change in the resistance for radii above 60 mm was observed. On the other hand, bending radii below 60 mm damaged some graphitic fibers in the CV thus increasing the overall resistance of the composite. Further, the 3DGS-CV composite was bent manually to 80, 60, and 20 mm radii multiple times, where no change in the electrical resistance was observed for bend radii of 60 and 80 mm after 30 bends. However, when bent at a 20 mm radius, resistance increased due to the failure of the brittle graphitic fibers, as shown in Figure S11 in the SI.

To summarize, the material characterization supported our hypothesis that extrusion of 3DGS into CV is possible and is the reason behind the lamination of these two materials. Furthermore, the arrangement and orientation of 3DGS and CV in the composite can be altered to harness the properties of the respective laminated structures for various applications. For example, one CV can be joined with one 3DGS via cold rolling, resulting in a lateral thermoelectric (TE) device without using a conductive medium like silver paste. More details and experimental results are described in the subsections below.

3.2. Thermoelectric and Photothermoelectric Characterization of 3DGS-CV Composites.

3DGS-CV Thermoelectric (TE) devices with various single or multiple P−N couples in different designs were fabricated and are shown in Figure 6. These designs are named here as TE1 (Figure 6a), TE2 (Figure 6b), and TE3 (Figure 6c), respectively. TE1 is a simple elbow-shaped joint between 3DGS and CV with the overlap area serving as a P−N couple where 3DGS and CV represent the legs of the TE composite. Figure 6b displays TE2 with two 3DGS legs welded to one common CV sheet, resulting in two P−N couples. Figure 6c shows a traditional Pi (Π) style lateral TE device, TE3 with three P−N couples.

TE1 with a 1 cm^2 couple area is heated or cooled during testing where the 1.5 cm long 3DGS and CV legs are kept outside the heating/cooling zone at room temperature and are used to record the open circuit voltage (V_{OC}). The V_{OC} is plotted against the temperature difference (ΔT) and is displayed in Figure 6d. This plot revealed a linear thermoelectric voltage output with an increase or decrease in the ΔT. For a P−N couple, a Seebeck coefficient of ∼ 32.5 μV K^{-1} was obtained using the created composites. This value is approximately equal to the Seebeck Coefficient of p-type 3DGS (S_p of +25 μV K^{-1}) minus the Seebeck coefficient of n-type CV (S_n of −6.8 μV K^{-1}) within the data uncertainty level of ∼±2 μV K^{-1}.

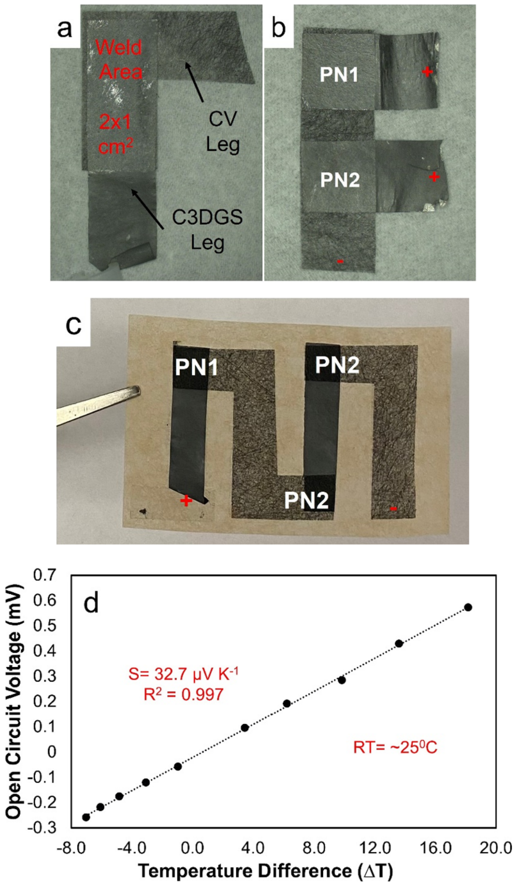

Figure 6. Optical image of (a) 3DGS-CV TE1 with 2 cm^2 overlap area; (b) 3DGS-CV TE2 with two 3DGS legs; (c) Π-shape (Pi) TE3 with 3 TE junctions; (d) Seebeck voltage vs temperature difference for TE1 shown in Figure 6a.

Furthermore, the effect of the couple area and the length of the legs on the TE behavior was tested. TE1 with 0.5, 1, and 2 cm^2 couple areas and leg lengths of 1.5 cm were exposed to ΔT of ∼16K (41.5 ± 1 °C at the couple) where the resultant V_{OC} from the fabricated devices is shown in Figure S12 of the SI. An increase in the overlap area required longer legs to maintain comparable ΔT and yielded similar V_{OC} to the composites with smaller overlap areas. The V_{OC} vs ΔT for the 0.5 cm^2 TE1 with 1.5 cm legs and 2 cm^2 TE1 with 3 cm legs are shown in

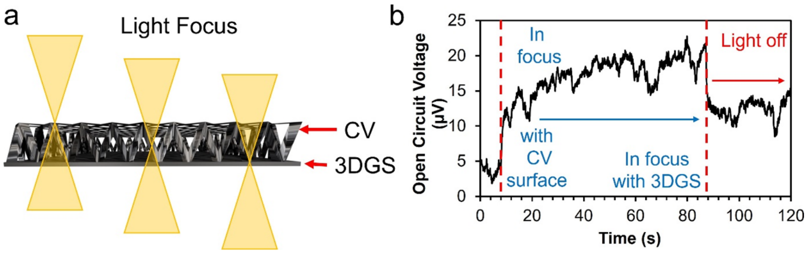

Figure 7. (a) Schematic illustrating the light beam focusing on the CV side of the composite for photothermoelectric response. (b) Voltage output from the 3DGS-CV composite when heated on the CV side of the composite using focused light.

Figure S13 of the SI. The data there revealed no influence of the P−N couple area on the thermovoltage.

Furthermore, the microinterfaces formed between 3DGS and CV were locally heated at random positions using a focused light source (spot size <5 μm^2) created by a Renishaw Raman microscope, as illustrated in Figure 7a. The light was concentrated by changing the focus from the top part of the CV toward the interface between 3DGS and CV. The voltage output due to the ΔT between the heated spot and the surrounding area was plotted and is shown in Figure 7b. The results from this experiment corroborated our hypothesis that every interface between graphitic fibers and 3DGS (as shown in Figure 3b) acts as an independent micro-TE couple.

When heated to ~41 °C, all tested composite devices yielded a ΔT of ~16 K. The power output and linear $I-V$ plot of TE1 with an overlap area of 1 cm^2 at an ΔT of 16 K are shown in Figure 8. The maximum power output ($P_{\text{max}} = 0.25 \times I_{\text{SC}} \times V_{\text{OC}}$[22,23]) recorded was 0.93 nW. Discussion on the thermoelectric power output for the composites TE1, TE2, and TE3 when heated with commercial TE modules is presented in Section S4 and Figure S14 of the SI. In summary, all the composites exhibited a similar thermovoltage of 535 μV at a ΔT of ~16 K. Though the overall overlap area for the TE2 shown in Figure 8 was 1 cm^2 (2 × 0.5 cm^2 overlap areas), a higher short circuit current of 9.25 μA was observed resulting in the highest power of 1.23 nW among all the tested devices.

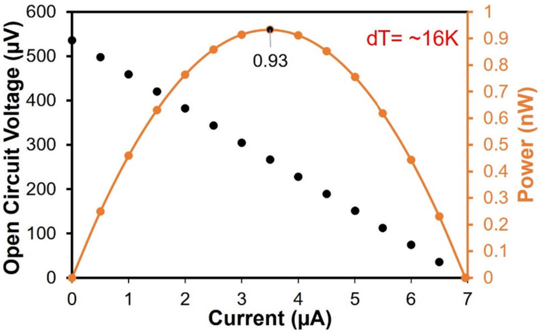

Figure 8. $I-V$ characteristics of TE1 with 1 cm^2 overlap along with power output.

It is published knowledge that both 3DGS and graphitic fibers are capable of absorbing electromagnetic (EM) radiation and demonstrate photothermoelectric (PTE) effect due to the photothermal-electrical transformation.[24,25] As shown in Figure S15 of the SI, no significant effect of the polyester binder in CV on the photothermal behavior of the 3DGS-CV composite was observed, since both sides revealed similar temperatures of about 61 °C when exposed to sunlight.

Composites TE1, TE2, and TE3 shown in Figure 6 were exposed to 1 Sun, i.e., 100 mW/cm^2 artificial radiation (generated by a Newport Solar simulator 67005) to understand the effect of design and overlap area on the PTE effect. A description of the test setup and the power output data is given in Section S5 of the SI. As shown in Figure S16a, TE2 revealed highest ΔT followed by 1 cm^2 TE1, TE3, and 0.5 cm^2 TE1 composites. This is due to the greater photoexposed area which resulted in a higher measured temperature. The V_{OC} of the II composite, TE3 showed the highest value as illustrated in Figure S16b, which was expected due to the "in series" arrangement, as discussed earlier. However, it suffered from higher resistance, causing a lower short-circuit current. The lower resistance of the double welded composite enhanced the short circuit current along with higher ΔT resulting in the highest power output of 1.19 nW, whereas the power output for TE3 was only 0.39 nW (Figure S16c). Furthermore, TE3 was slightly modified, as shown in Figure S16d, and referred to here as the Pi (II) device. Such a design allowed only exposure of the TE junctions, thus insulating the rest. The achieved better insulation slightly lowered the temperature of the legs by about 1.7K, resulting in the highest open circuit voltage with increased short circuit current and power of 0.57 nW.

The power output and other properties of 3DGS-CV composites have been compared with those of various carbon-based TE materials when heated or exposed to electromagnetic radiation. The gathered-from-the-literature information along with data from this work are shown in Tables S1 and S2 of the SI. There, one can notice that our 3DGS-CV composite revealed better performance than many graphene and CNT-based materials. However, 3DGS-CV fell short in comparison with various "chemically doped" graphene and CNT composites. Increasing the Seebeck coefficient of 3DGS by doping, also decreasing the interfacial weld resistance, and creating multiple P−N couples may result in a higher power output.

3.3. Effect of Moisture on the Performance of the 3DGS-CV Composite. When exposed to oxidizing or reducing environment, a change in electrical and thermoelectric behavior of graphene, reduced graphene oxide (rGO), and carbon nanotubes (CNT) has been reported due to the created deficiency of either holes or electrons. The moisture content in the air significantly affected the thermoelectric n-type behavior.[26−28] Water molecules adsorbed on carbon materials induce a p-type behavior due to the electron-withdrawing groups where n-type rGO develops a p-type characteristic when exposed to moisture.[29−31] Further, the severe effect of moisture on the poly(ethylene imine) (PEI) doped CNT was also reported.[32] Here, the thermoelectric stability of hydrophobic 3DGS, CV, and TE1 was tested in a controlled environment with varying relative humidity (RH). Details about this experiment are given in Section S6 of the SI.

Thermovoltage and ΔT across the 3DGS and 0.3 CV with changing RH are shown in Figure S17 of the SI. Furthermore, the test results for the TE1 are displayed in Figure 9. 3DGS and CV demonstrated high stability at a wide range of RH. It should be noted that 3DGS is a p-type material with a good amount of moisture adsorbed on it[30,31]; hence, there may not be a huge effect on its TE behavior. Further, unlike various n-type materials from the literature, CV revealed a stable n-type behavior, even at a high RH of 81%. This may be due to the polyester binder protecting the CV from humidity.

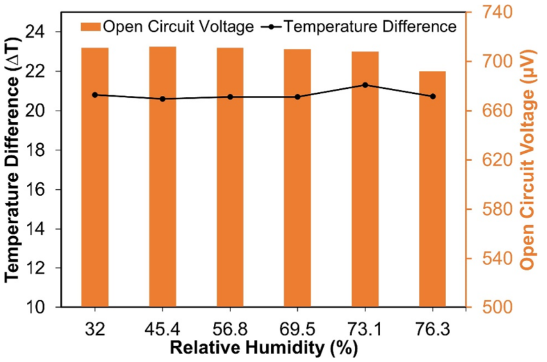

Figure 9. Effect of relative humidity (RH) on the thermovoltage and ΔT of the TE1 3DGS-CV composite at room temperature.

With an increase in RH, no significant change in the TE behavior of TE1 was observed. Above ~73% RH, the thermovoltage of the composite decreased, which could be either due to an increase of hole density in a CV or because of its wetting causing a lower ΔT. A similar trend was also observed for CV (Figure S17b) where above 72.2% RH, a decrease in thermovoltage was recorded. From these tests, it is clear that 3DGS, CV, and 3DGS-CV composites are stable at a wide range of temperatures and RH. The aging stability of the 3DGS-CV composite in an ambient environment was tested every week for a month and the obtained data are shown in Figure S18. The results there corroborate the high stability of the composite where no change in its thermovoltage or Seebeck coefficient was observed after a month.

3.4. Flexible and Thin 3DGS-CV Composites as Thermal Sensors. Various carbon materials were explored as thermal sensors relying on either a change in electrical resistance or the Seebeck effect. Table S3 in the SI lists a few of them. The compositès resistance can be altered by varying stress/strain and temperature. Complex situations involving stress/strain and higher temperature to change the electrical resistance may not be a very reliable approach for measuring the temperature. On the other hand, measurement based on the Seebeck effect is trustworthy as the V_{OC} depends on the ΔT and not on the change in resistance. Stress and strain may not affect the measured output unless the structure of the material is highly altered. 3DGS-CV composites appear to be a good candidate for temperature sensing and mapping because of the earlier indicated advantages including ease of 3DGS synthesis, commercial availability of CV, high resistance to humidity, pronounced TE/PTE response to temperature change, and thin, flexible profile enabling straightforward design and patterning. 3DGS-CV thermocouples (TC) with single or double welds were manufactured and are shown in Figure 10a,b. The CV legs were aligned along the length of a cardboard piece where the 3DGS legs were folded behind the cardboard. Both legs were connected to copper conductors for measuring voltage/current. Here cardboard was used to prevent the heating of graphene legs.

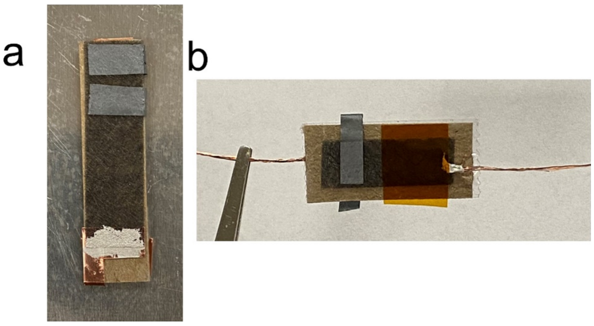

Figure 10. (a) Double weld TC. (b) Single weld mini-TC.

The response of the 3DGS-CV TC to heat was instantaneous. A fast voltage response (1 s) due to tapping and briefly touching the P—N junction with a finger covered with a glove was observed, as displayed in Figure S19a. This reaction suggests the potential application of TCs as a heat flux or touch sensor. Further, 3DGS-CV TCs can be embedded into various types of fabric by using a variety of sewing techniques including ultrasound sewing. A mini version of the TC with a single P—N couple and legs insulated by Kapton is displayed in Figure 10b. In this work, the composite TCs were tested for two applications: tracking of human breath and battery temperature monitoring. For the first application, the composite was kept inside a medical facemask near the upper lip where the temperature during "breath-in" and "out" resulted in a generation of thermovoltage, as illustrated in Figure S19b. Cooling due to air intake during "breath-in" decreased the temperature, while warm air during "breath-out" raised the temperature, resulting in a decrease and increase of thermovoltage, respectively. Figure S19b shows a reduction in thermovoltage when the P—N couple is moved away from the nose due to the decrease in temperature of the breath.

With the current expansion in the use of electronic devices and vehicles, there is a huge demand for batteries with a higher energy density, long battery life, and faster charging speeds. Batteries undergo mechanical, electrical (overcharging and overdischarging), and thermal (high-temperature work conditions) abuse often leading to thermal runaway, which is a major reason behind batteries catching fire.[33,34] The temperature of the batteries is used as a key factor to examine their health and prevent thermal runaway. Here by taking advantage of the thin composite profile along with the ability to customize the P—N couple area and the length of the legs, we were able to demonstrate using 3DGS-CV TC for surface temperature monitoring of a 500 mA h Li-ion battery (purchased from Adafruit Industries) during charging and discharging at constant currents. The battery was cycled at a charge—discharge rate of 1C (0.5 A), 1.5C (0.75 A), and 2C (1 A) between 4.5 and 2.7 V using a Gamry Interface 1000. Before the test, the battery was completely discharged at 1C. The current used for charging and discharging the battery and the respective voltage vs time plot are shown in Figure 11a,b, respectively.

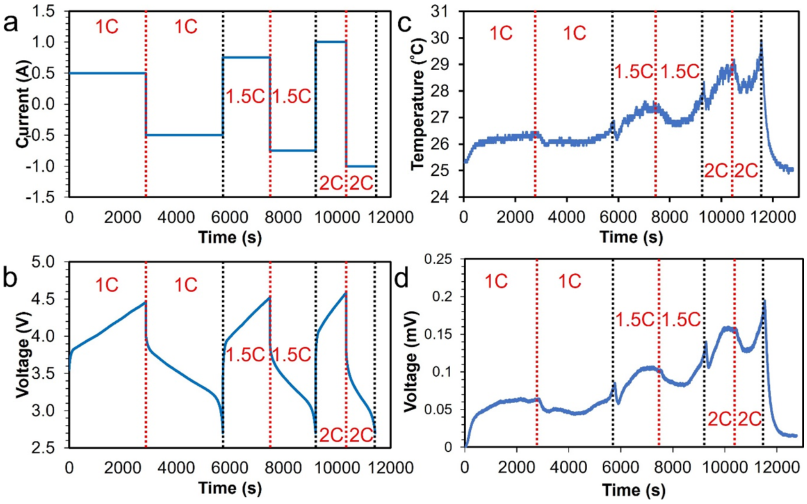

Figure 11. (a) Current profile used to charge and discharge the battery. (b) Voltage profile of the battery during charging and discharging. (c) Temperature of the battery during the charge−discharge cycles recorded using a standard K-type TC. (d) Thermoelectric response of the single weld TC attached on a Li-ion battery during the charge−discharge cycles.

The temperature profile from the K-type thermocouple along with the voltage output from the TE composite are shown in Figure 11c,d, respectively. From these plots, the performance of the composite TC is good where small temperature changes are also captured. An increase in temperature with C rate is observed which is expected due to faster reaction kinetics.[35] High temperatures with sharp peaks were observed at the end of each discharge curve (highlighted black dotted lines in Figure 11c,d) due to an abrupt sudden drop in voltage reaching the minimum value of 2.7 V.[35]

3.5. 3DGS-CV Composites with Multiple P−N Couples for Temperature Mapping. Furthermore, the composites with multiple P−N junctions shown in Figure 12a,b were studied for two-zone temperature mapping. During the testing of both the composites, as highlighted with red dotted boxes, P−N junctions were kept on two separate TE heaters, where the legs highlighted with white dotted boxes were retained away from the heaters at room temperature. In the first arrangement shown in Figure 12a, the CV legs are connected via one 3DGS and are connected to two different terminals. In the second arrangement shown in Figure 12b, the 3DGS legs were connected to two separate probes of the same terminal, where the CV leg was connected to other terminals to complete the circuit for voltage/current recording. The P−N junctions of the TE composite shown in Figure 12a were heated separately to two different temperatures, and the acquired voltage output is shown in Figure 12c,d. The heating pattern described in Table 2 was used for the conducted tests.

The heating pattern from Table 2 was repeated multiple times, which resulted in a similar voltage output profile, as shown in Figure 12c. Furthermore, a complex heating pattern was also tested where the resultant voltage output along with the PN1 and PN2 temperatures for the individual profile zones is displayed in Figure 12d. Based on these voltage output profiles, the composite shown in Figure 12a displayed an NP-PN device behavior. On the other hand, the voltage output profile along with the respective temperatures (heating pattern discussed in Table 2) of PN1 and PN2 with the same composite design, as shown in Figure 12b and a 3 cm gap between the junctions, is displayed in Figure 12e. From the voltage output plots, it is obvious that this composite exhibited a distinct behavior than the earlier one.

Although both designs can map different temperatures across two heating zones, the composite shown in the first arrangement is limited to two terminals and is not scalable. The second design can be scaled to larger dimensions with multiple P−N junctions to monitor numerous independent temperature zones. This opportunity is explored here, and the results are displayed in Figure 12f. A 3DGS-CV composite with 3 P−N couples with a 1 cm gap between the couple was used to map temperatures across an aircraft's wing of an F16 toy to detect ice formation. The CV was connected to the negative terminals where the individual graphene legs were wrapped under the wing and were connected to the positive terminals individually to enable temperature mapping. The testing of the shown composite was done separately where small cool packs, purchased from Uline, were used to simulate icing and to locally cool individual/multiple TE 3DGS-CV P−N junctions. The voltage output when one vs two vs three junctions were cooled is shown in Figure 12g.

4. CONCLUSIONS

This work demonstrates a new processing approach to join three-dimensional graphene (3DGS) with a commercially available carbon veil (CV) via cold rolling. Extensive characterization revealed bulk extrusion of 3DGS into CV caused by this procedure and the formation of many microinterfaces due to compressive stress. The fabricated 3DGS-CV composite exhibited good flexibility, thermal stability, and tensile strength. Due to the P-type and N-type behaviors of 3DGS and CV, respectively, the 3DGS-CV couples with a Seebeck coefficient of 32.5 μV/K were recorded. The microinterfaces showed independent thermoelectric behavior with a very good response to light and heat. The simple cold rolling procedure allowed the making of scalable composites with large dimensions and multiple P−N couples. Though a relatively lower power output was observed, the ease of synthesis and fabrication including high stability at a wide range of temperatures and relative humidity make the 3DGS-CV composite a good candidate for energy applications, particularly for low-power and wearable electronics. Further-

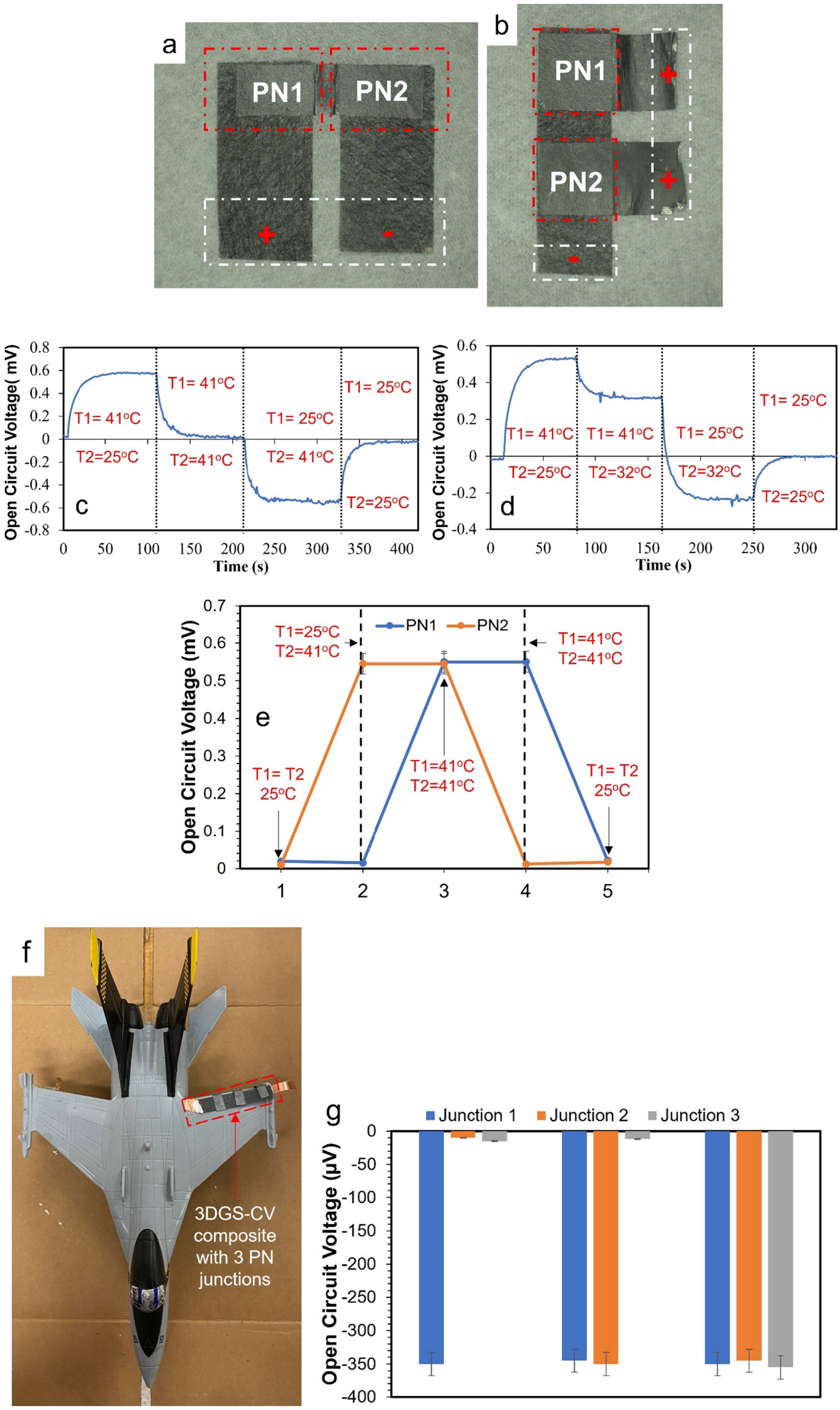

Figure 12. (a, b) Two types of composites with red boxes indicating the heated regions where the white boxes represent room temperature. (c) Voltage output vs time of the composite shown in Figure 12a due to the heating profile shown in Table 2. (d) Voltage vs time of the composite shown in Figure 12a at different heating temperatures either 41 or 32 °C. (e) Thermoelectric voltage output vs time of the composite shown in Figure 12b due to the heating profile discussed in Table 2. (f) F16 toy plane with the 3DGS-CV composite for temperature mapping across the wing. (g) Voltage output from different TE junctions when cooled independently.

Table 2. Heating Pattern Used To Change the Temperature of P−N Junctions PN1 and PN2 of the Composites

	temperature (°C)				
PN junction	step 1	step 2	step 3	step 4	step 5
PNI	RT	41	41	RT	RT
PN2	RT	RT	41	41	RT

more, the simple 3DGS-CV devices created here enabled reliable and reproducible temperature monitoring of a Li-ion battery including large area multizone temperature mapping.

■ ASSOCIATED CONTENT

Supporting Information

The Supporting Information is available free of charge at https://pubs.acs.org/doi/10.1021/acsami.3c19605.

> FTIR spectra of CV with various densities in comparison with carbon paper; stress−strain plot for 0.3 g/cm^3 CV; details about the Seebeck coefficient, electrical conductivity, and force during cold rolling measurement setups along with the raw Seebeck data for 3DGS and CV materials; XRD spectra of 3DGS-CV composite and 3DGS; VOIGT peak fitting of Raman 2D peak for extruded 3DGS and C3DGS; TGA of 3DGS, 0.3 CV, and 3DGS-CV composite; effect of multiple bends on the resistance of the 3DGS-CV composite; thermoelectric and photothermoelectric power output details from TE1, TE2, and TE3 along with the raw data V_{OC} vs ΔT for TE1 with 0.5 and 2 cm^2 overlap areas; tables comparing the power output of 3DGS-CV composites with various doped and undoped carbon TE materials when exposed to heat or light; effect of relative humidity on the TE behavior of 3DGS and CV along with data on the long-term stability of the 3DGS-CV composite; and table comparing various carbon-based thermocouples reported in the literature along with their mode of temperature sensing and the techniques used to manufacture them; response of 3DGS- CV composite TC to finger tapping and human breath (PDF)

■ AUTHOR INFORMATION

Corresponding Author

Vesselin Shanov − *Department of Mechanical and Materials Engineering and Department of Chemical and Environmental Engineering, University of Cincinnati, Cincinnati 45221 Ohio, United States;* orcid.org/0000-0002-0041-7821; Email: shanovvn@ucmail.uc.edu

Authors

Vamsi Krishna Reddy Kondapalli − *Department of Mechanical and Materials Engineering, University of Cincinnati, Cincinnati 45221 Ohio, United States;* orcid.org/0000-0002-0539-7102

Oluwasegun Isaac Akinboye − *Department of Mechanical and Materials Engineering, University of Cincinnati, Cincinnati 45221 Ohio, United States*

Yu Zhang − *Department of Mechanical and Materials Engineering, University of Cincinnati, Cincinnati 45221 Ohio, United States;* orcid.org/0000-0003-2355-616X

Guillaume Donadey − *Unite de Formation de Chimie, University of Bordeaux, Talence 33405 Gironde, France*

Justin Morrow − *Thermo Fisher Scientific, Madison 53711 Wisconsin, United States; Department of Environmental and Public Health Sciences, University of Cincinnati, Cincinnati 45221 Ohio, United States*

Kyle Brittingham − *Department of Chemical and Environmental Engineering, University of Cincinnati, Cincinnati 45221 Ohio, United States*

Ayush Arun Raut − *Department of Mechanical and Materials Engineering, University of Cincinnati, Cincinnati 45221 Ohio, United States*

Mahnoosh Khosravifar − *Department of Mechanical and Materials Engineering, University of Cincinnati, Cincinnati 45221 Ohio, United States*

Bashar Al-Riyami − *Department of Chemical and Environmental Engineering, University of Cincinnati, Cincinnati 45221 Ohio, United States;* orcid.org/0000-0002-2311-1868

Je-Hyeong Bahk − *Department of Mechanical and Materials Engineering, University of Cincinnati, Cincinnati 45221 Ohio, United States;* orcid.org/0000-0002-5808-2227

Complete contact information is available at: https://pubs.acs.org/10.1021/acsami.3c19605

Notes

The authors declare no competing financial interest.

■ ACKNOWLEDGMENTS

This study was partially supported by the National Institute for Occupational Safety and Health through grant #T42OH008432 from the Pilot Research Project Training Program of the University of Cincinnati (UC) Education and Research Center. One of the authors, V. K. R. K., is grateful for the financial support provided by grant #WSIC23-220513-010 from the State of Ohio. The authors also acknowledge the financial support from the UC Collaborative Research Advancement grant #1018371. O. A., Y. Z., and J.-H. B. recognize the financial support from the National Science Foundation under Grants No. 1905571. The authors would like to acknowledge the help of Dr. Melodie Fickenscher at the UC Advanced Materials Characterization Center, and Dr. Necati Kaval at the Chemical Sensors, and Biosensors Instrumentation Facility for his help with FTIR. The use of a in situ prototype Raman spectroscopy instrument provided by Thermo Fisher Scientific in collaboration with the UC Advanced Materials Characterization Center is also recognized.

■ REFERENCES

(1) Zhu, Y.; Murali, S.; Cai, W.; Li, X.; Suk, J. W.; Potts, J. R.; Ruoff, R. S. Graphene and Graphene Oxide: Synthesis, Properties, and Applications. *Adv. Mater.* **2010**, *22* (35), 3906−3924.

(2) Zhang, F.; Yang, K.; Liu, G.; Chen, Y.; Wang, M.; Li, S.; Li, R. Recent Advances on Graphene: Synthesis, Properties and Applications. *Compos Part A Appl. Sci. Manuf.* **2022**, *160*, No. 107051.

(3) Mohan, V. B.; Lau, K t.; Hui, D.; Bhattacharyya, D. Graphene-Based Materials and their Composites: A Review on Production, Applications and Product Limitations. *Composites, Part B* **2018**, *142*, 200−220.

(4) Huang, X.; Qi, X.; Boey, F.; Zhang, H. Graphene-Based Composites. *Chem. Soc. Rev.* **2012**, *41* (2), 666−686.

(5) Ramírez, C.; Shamshirgar, A. S.; Pérez-Coll, D.; Osendi, M. I.; Miranzo, P.; Tewari, G. C.; Karppinen, M.; Hussainova, I.; Belmonte, M. CVD Nanocrystalline Multilayer Graphene Coated 3D-Printed Alumina Lattices. *Carbon N Y.* **2023**, *202*, 36−46.

(6) Madito, M. J.; Matshoba, K. S.; Ochai-Ejeh, F. U.; Mongwaketsi, N.; Mtshali, C. B.; Fabiane, M.; Manyala, N. Nickel-Copper Graphene Foam Prepared by Atmospheric Pressure Chemical Vapour

Deposition for Supercapacitor Applications. *Surf. Coat. Technol.* **2020**, *383*, No. 125230.

(7) Wang, H.; Ma, C.; Zhang, W.; Cheng, H. M.; Zeng, Y. Improved Damping and High Strength of Graphene-Coated Nickel Hybrid Foams. *ACS Appl. Mater. Interfaces* **2019**, *11*, 42690−42696, DOI: 10.1021/ACSAMI.9B10382.

(8) Wang, M.; Duan, X.; Xu, Y.; Duan, X. Functional Three-Dimensional Graphene/Polymer Composites. *ACS Nano* **2016**, *10* (8), 7231−7247.

(9) Xiao, W.; Li, B.; Yan, J.; Wang, L.; Huang, X.; Gao, J. Three Dimensional Graphene Composites: Preparation, Morphology and their Multi-Functional Applications. *Compos Part A Appl. Sci. Manuf.* **2023**, *165*, No. 107335.

(10) Sun, Z.; Fang, S.; Hu, Y. H. 3D Graphene Materials: From Understanding to Design and Synthesis Control. *Chem. Rev.* **2020**, *120* (18), 10336−10453.

(11) Li, J. T.; Stanford, M. G.; Chen, W.; Presutti, S. E.; Tour, J. M. Laminated Laser-Induced Graphene Composites. *ACS Nano* **2020**, *14* (7), 7911−7919.

(12) Wang, B.; Li, Z.; Wang, C.; Signetti, S.; Cunning, B. V.; Wu, X.; Huang, Y.; Jiang, Y.; Shi, H.; Ryu, S.; Pugno, N. M.; Ruoff, R. S. Folding Large Graphene-on-Polymer Films Yields Laminated Composites with Enhanced Mechanical Performance. *Adv. Mater.* **2018**, *30* (35), No. 1707449.

(13) Marsden, A. J.; Papageorgiou, D. G.; Vallés, C.; Liscio, C.; Palermo, V.; Bissett, M. A.; Young, R. J.; Kinloch, I. A. Electrical Percolation in Graphene−Polymer Composites. *2D Mater.* **2018**, *5* (3), No. 032003.

(14) Mao, S.; Lu, G.; Chen, J. Three-Dimensional Graphene-Based Composites for Energy Applications. *Nanoscale.* **2015**, *7* (16), 6924−6943.

(15) Kondapalli, V. K. R.; He, X.; Khosravifar, M.; Khodabakhsh, S.; Collins, B.; Yarmolenko, S.; Paz y Puente, A.; Shanov, V. CVD Synthesis of 3D-Shaped 3D Graphene Using a 3D-Printed Nickel−PLGA Catalyst Precursor. *ACS Omega* **2021**, *6* (43), 29009−29021.

(16) DeArmond, D.; Zhang, L.; Malik, R.; Vamsi Krishna Reddy, K.; Alvarez, N.; Haase, M. R.; Hsieh, Y. Y.; Kanakaraj, S. N.; Oslin, N.; Bruneman, J.; Daum, J.; Shanov, V. Scalable CVD Synthesis of Three-Dimensional Graphene from Cast Catalyst. *Mater. Sci. Eng., B* **2020**, *254*, No. 114510.

(17) Chen, Z.; Ren, W.; Gao, L.; Liu, B.; Pei, S.; Cheng, H. M. Three-Dimensional Flexible and Conductive Interconnected Graphene Networks Grown by Chemical Vapour Deposition. *Nat. Mater.* **2011**, *10* (6), 424−428.

(18) Kondapalli, V. K. R.; Zhang, G.; Zhang, Y.; Khosravifar, M.; Brittingham, K.; Phan, N.; Yarmolenko, S.; Bahk, J. B.; Shanov, V. New Architecture of 3D Graphene with Enhanced Properties Obtained by Cold Rolling. *Carbon N Y.* **2023**, *207*, 116−128.

(19) Bhattacharya, S. S.; Chaudhari, S. B. Study on Structural, Mechanical and Functional Properties of Polyester Silica Nanocomposite Fabric. *Int. J. Pure Appl. Sci. Technol.* **2014**, *21* (1), 43−52. www.ijopaasat.in Accessed June 13, 2023

(20) Polyester − Database of ATR-FT-IR spectra of various materials. https://spectra.chem.ut.ee/textile-fibres/polyester/ (accessed June 2023).

(21) Roscher, S.; Hoffmann, R.; Ambacher, O. Determination of the Graphene-Graphite Ratio of Graphene Powder by Raman 2D Band Symmetry Analysis. *Anal. Methods* **2019**, *11* (9), 1224−1228.

(22) Rafique, S.; Burton, M. R.; Badiei, N.; Gonzalez-Feijoo, J.; Mehraban, S.; Carnie, M. J.; Tarat, A.; Li, L. Lightweight and Bulk Organic Thermoelectric Generators Employing Novel P-Type Few-Layered Graphene Nanoflakes. *ACS Appl. Mater. Interfaces* **2020**, *12* (27), 30643−30651.

(23) Rafique, S.; Burton, M. R.; Badiei, N.; Gonzalez-Feijoo, J.; Mehraban, S.; Carnie, M. J.; Tarat, A.; Li, L. Paper Thermoelectrics by a Solvent-Free Drawing Method of All Carbon-Based Materials. *ACS Omega* **2021**, *6* (7), 5019−5026.

(24) Jin, X. Z.; Li, H.; Wang, Y.; Zy, Yang; Qi, X. D.; Yang, J. H.; Wang, Y. Ultraflexible PEDOT:PSS/Helical Carbon Nanotubes Film for All-in-One Photothermoelectric Conversion. *ACS Appl. Mater. Interfaces* **2022**, *14* (23), 27083−27095.

(25) Wang, H.; Wang, R.; Chen, C.; Zhou, Z.; Liu, J. W. Manipulating Single-Walled Carbon Nanotube Arrays for Flexible Photothermoelectric Devices. *JACS Au* **2022**, *2* (10), 2269−2276.

(26) Kong, J.; Franklin, N. R.; Zhou, C.; Chapline, M. G.; Peng, S.; Cho, K.; Dai, H. Nanotube Molecular Wires as Chemical Sensors. *Science* **2000**, *287* (5453), 622−625.

(27) Na, P. S.; Kim, H.; So, H. M.; Kong, K. J.; Chang, H.; Ryu, B. H.; Choi, Y.; Lee, J. O.; Kim, B. K.; Kim, J. J.; Kim, J. Investigation of the Humidity Effect on the Electrical Properties of Single-Walled Carbon Nanotube Transistors. *Appl. Phys. Lett.* **2005**, *87*, No. 093101.

(28) Han, J. W.; Kim, B.; Kobayashi, N. P.; Li, J.; Meyyappan, M. A Simple Method for the Determination of Doping Type in Nanomaterials Based on Electrical Response to Humidity. *Appl. Phys. Lett.* **2012**, *101*, 14.

(29) Tu, N. D. K.; Lim, J. A.; Kim, H. A Mechanistic Study on the Carrier Properties of Nitrogen-Doped Graphene Derivatives using Thermoelectric Effect. *Carbon N Y.* **2017**, *117*, 447−453.

(30) Wehling, T. O.; Novoselov, K. S.; Morozov, S. V.; Vdovin, E. E.; Katsnelson, M. I.; Geim, A. K.; Lichtenstein, A. I. Molecular doping of graphene. *Nano Lett.* **2008**, *8* (1), 173−177.

(31) Melios, C.; Giusca, C. E.; Panchal, V.; Kazakova, O. Water on Graphene: Review of Recent Progress. *2D Mater.* **2018**, *5* (2), No. 022001.

(32) Yasunishi, T.; Kishimoto, S.; Ohno, Y. Effect of Ambient Air on n-type Carbon Nanotube Thin-Film Transistors Chemically Doped with Poly(Ethylene Imine). *Jpn. J. Appl. Phys.* **2014**, *53*, No. 05FD01. (5 SPEC. ISSUE 1):

(33) Kong, D.; Lv, H.; Ping, P.; Wang, G. A Review of Early Warning Methods of Thermal Runaway of Lithium Ion Batteries. *J. Energy Storage.* **2023**, *64*, No. 107073.

(34) Liao, Z.; Zhang, S.; Li, K.; Zhang, G.; Habetler, T. G. A Survey of Methods for Monitoring and Detecting Thermal Runaway of Lithium-Ion Batteries. *J. Power Sources.* **2019**, *436*, No. 226879.

(35) Mutyala, M. S. K.; Zhao, J.; Li, J.; Pan, H.; Yuan, C.; Li, X. In-Situ Temperature Measurement in Lithium Ion Battery by Transferable Flexible Thin Film Thermocouples. *J. Power Sources.* **2014**, *260*, 43−49.